Doping-induced spin reorientation and magnetic phase diagram of EuMn$_{1-x}$Zn$_x$Sb$_2$ (0 ⩽ x ⩽ 1)

Yuanying Xia,[1,*] Lin Wang ●,[2,*] Yan Liu,[3] Liyu Zhang,[1] Xueliang Wu,[1] Long Zhang,[1] Tianran Yang,[1] Kunya Yang,[1]
Mingquan He,[1] Yisheng Chai,[1] Xiaoyuan Zhou,[1,†] and Aifeng Wang ●[1,‡]

[1]*Low Temperature Physics Laboratory, College of Physics and Center of Quantum Materials and Devices,
Chongqing University, Chongqing 401331, China*
[2]*Department of Physics, University of Konstanz, D-78457 Konstanz, Germany*
[3]*Analytical and Testing Center, Chongqing University, Chongqing 401331, China*

EuMnSb$_2$ is an intriguing magnetic topological semimetal containing two antiferromagnetic sublattices, and the interplay of magnetism between Eu and Mn sublattices leads to rich interesting transport phenomena. Here we report a comprehensive experimental study of the magnetic properties in EuMn$_{1-x}$Zn$_x$Sb$_2$ (0 ⩽ x ⩽ 1) by using structural, resistivity, magnetization, and specific heat measurements. The magnetic phase diagrams of EuMn$_{1-x}$Zn$_x$Sb$_2$ along two magnetic field orientations are established based on magnetization and specific heat measurements, constituted by the antiferromagnetic ordering of Mn at high temperature, and successive magnetic transitions of Eu at low temperatures. The antiferromagnetic transition temperature of Mn is suppressed by Zn doping and cannot be detected by specific heat measurements when $x > 0.3$. The antiferromagnetic transition temperature of Eu exhibits a weak nonmonotonic doping dependence with a significant anisotropy in the doping range of 0 ⩽ x ⩽ 0.4. The spin orientation of Eu is gradually reoriented from the out-of-plane direction to the in-plane direction. It closely correlates with the Mn antiferromagnetic ordering, indicating a strong coupling between the Eu and Mn magnetism. Our study will be helpful for understanding the magnetic properties of compounds with two antiferromagnetic lattices and open an avenue for tuning the spin orientation through the interaction between the different magnetic lattices.

I. INTRODUCTION

Magnetic topological materials have attracted intense attention in the field of spintronics since they pave a new avenue to control electronic transport properties by utilizing the interplay between magnetism and topology [1,2]. The layered square-net-based compounds, AMnPn_2 (A = Ca, Sr, Ba, Eu, or Yb; Pn = Sb or Bi), are promising candidates for the investigation of magnetic topological semimetals due to the diversities of both structure and magnetism [3]. Among these AMnPn_2 materials, EuMnSb$_2$ is of particular interest as it contains two antiferromagnetic (AFM) sublattices. Therefore EuMnSb$_2$ exhibits richer transport phenomena, i.e., colossal anisotropic magnetoresistance (AMR) [4], large spin entropy enhanced thermopower [5], strong coupling between Eu magnetism, and band topology [6] and so on.

The magnetic structure of EuMnSb$_2$ has recently been intensively investigated by neutron measurements [7–10], which is composed of C-type AFM ordering of Mn^{2+} below 350 K and possibly A-type AFM ordering of Eu^{2+} below 20 K. The C-type AFM ordering of Mn with moments along a axis (out-of-plane direction) has already been confirmed by various neutron measurements [7–10]. However,

whether the magnetic structure of the Eu sublattice has A-type AFM ordering remains elusive. The detailed magnetic structure, including the stacking sequence and the canting angle, was reported to be conflicting in the previous literature [7–10]. Therefore it is crucial to clarify the magnetic properties in EuMnSb$_2$ to understand and manipulate the magnetic structure and related physical properties. Spatially separation between Eu and Mn layers in EuMnSb$_2$ allows tuning the magnetic sublattice separately by chemical doping. The isovalent nonmagnetic doping is one of the effective ways to control the magnetic coupling through the dilution effect [11]. Then, the role of the magnetic element can be revealed by comparing physical phenomena between samples with different magnetic element concentrations. Very recently, Zhang *et al.* reported a comprehensive experimental investigation on Eu$_{1-x}$Sr$_x$MnSb$_2$, which revealed that the Eu spin orientation and related quantum transport properties of EuMnSb$_2$ could be effectively tuned by nonmagnetic isovalent Sr doping on Eu site [9].

In this paper, we, on the other hand, study the magnetic properties of EuMnSb$_2$ by using the nonmagnetic isovalent Zn doping on the Mn site. The substitution of Mn can help us to deepen the understanding of the role of Mn in AMnPn_2 compounds, which remains largely elusive in previous papers. In addition, the Eu magnetic states can be effectively tuned through the variation of Eu-Mn coupling. Here, we successfully synthesized a series of high-quality EuMn$_{1-x}$Zn$_x$Sb$_2$ (0 ⩽ x ⩽ 1) single crystals via the self-flux method, which

---
*These authors contributed equally to this work.
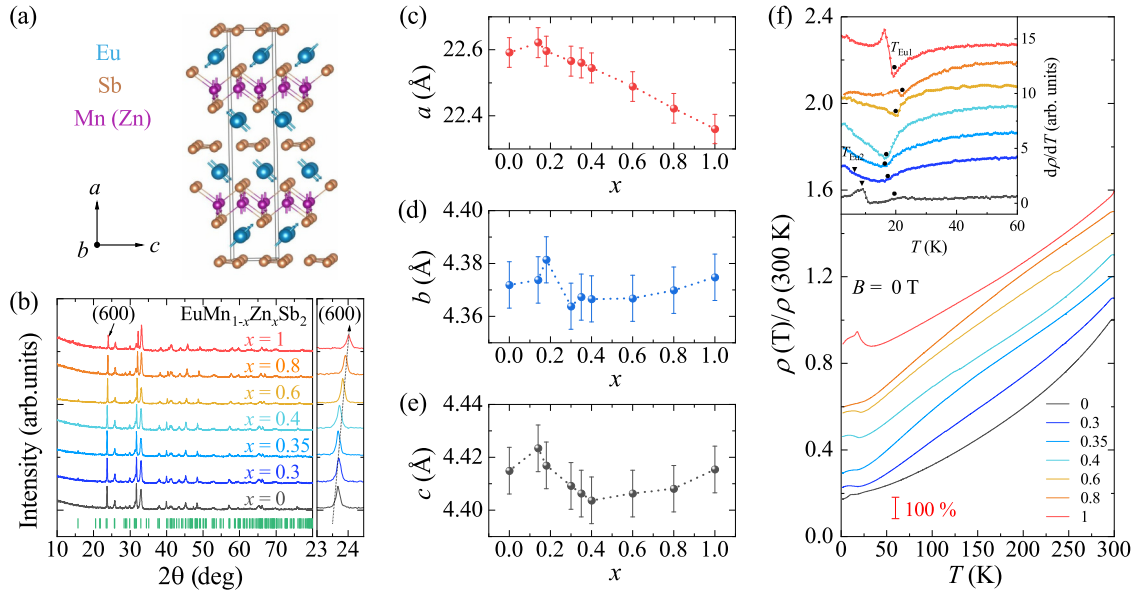†xiaoyuan2013@cqu.edu.cn
‡afwang@cqu.edu.cn

FIG. 1. (a) The crystal and magnetic structure of $EuMnSb_2$, the gray lines indicate the unit cells. The magnetic structure of $EuMnSb_2$ consists of an Mn sublattice with a C-type AFM and an Eu sublattice with a canted A-type AFM. Note that the orientation and stacking sequence of Eu depends on temperature, magnetic field, and Zn content x. (b) The powder XRD patterns of the $EuMn_{1-x}Zn_xSb_2$ ($0 \leqslant x \leqslant 1$). The right panel shows (600) diffraction peak. (c)–(e) show the refined lattice parameters (a, b, and c) as a function of Zn content x, respectively. (f) The normalized zero-field in-plane electrical resistivity as a function of temperature for the $EuMn_{1-x}Zn_xSb_2$. Note that each subsequent resistivity is shifted upward by 100% for clarity. The inset shows the first derivative of resistivity $d\rho/dT$.

was systematically characterized by structural, transport, specific heat, and magnetization measurements. The in-plane and out-of-plane magnetic phase diagrams of $EuMn_{1-x}Zn_xSb_2$ with respect to Zn content and temperature are established based on the results of magnetization and specific heat measurements. The magnetic states are separated by the Zn-doping dependence of T_{Mn}, T_{Eu1}, and T_{Eu2}, where T_{Mn}, T_{Eu1}, and T_{Eu2} are the transition temperatures corresponding to Mn AFM, Eu AFM, and Eu spin reorientation, respectively. We find that T_{Mn} is suppressed by Zn doping, whereas T_{Eu1} almost keeps intact in the entire doping range. As for T_{Eu2}, it first decreases with increasing x and then disappears when $x > 0.3$. Moreover, the orientation of Eu gradually changes from a direction close to the a axis (out-of-plane direction) to the bc plane (in-plane direction) with increasing Zn content, caused by a strong to weak coupling between Eu and Mn sublattices.

II. EXPERIMENTAL DETAILS

Single crystals of $EuMn_{1-x}Zn_xSb_2$ with $0 \leqslant x \leqslant 1$ were grown via the self-flux method using excess Sb as flux. Eu lumps (99.99%), Mn pieces (99.8%), Zn grains (99.995%), and Sb lumps (99.99%) are used as starting materials. The starting materials were mixed according to the mole ratio Eu:Mn:Zn:Sb = $1:1-x:x:4$. The mixture was placed into an alumina crucible and then sealed in a quartz tube under vacuum. The quartz tubes were slowly heated to 1050 °C in 10 h, held at 1050 °C for 10 h, followed by subsequent cooling to 680 °C at a rate of 2.5 °C/h. Once the furnace reaches 680 °C, shiny single crystals with typical dimensions of $4 \times 3 \times 1$ mm^3 can be obtained by decanting the excess flux using a centrifuge. The single crystals are relatively stable in the air for at least 6 hours.

Powder x-ray diffraction (XRD) measurements were carried out in a PANalytical powder diffractometer (Cu k_α = 1.5406 Å radiation) to characterize the crystal structure. The chemical compositions of single crystals were determined by energy-dispersive x-ray spectroscopy (EDS) measurements in a Thermo Fisher Quattro S Environmental scanning electron microscope. The correlation between the EDS determined actual Zn content x_{EDS} and nominal Zn content x_{nom} is illustrated by an x_{EDS} versus x_{nom} plot as shown in Fig. S1(a) of Ref. [12]. Note that x_{EDS} is significantly higher than x_{nom} in the underdoped region. The difference between x_{EDS} and x_{nom} decreases as x_{nom} increases, and $x_{EDS} \simeq x_{nom}$ can be observed when $x \geqslant 0.6$. The Zn content x hereafter represents the actual composition x_{EDS} in this paper. The in-plane resistivity was measured in a TeslatronPT magnet (Oxford Instruments-14T). The electrical contacts were made to the sample in a standard four-probe configuration. Heat capacity was measured in a Quantum Design DynaCool Physical Properties Measurement System (PPMS-9T). Magnetization data were collected in a PPMS-9T using the VSM option.

III. RESULTS AND DISCUSSION

A. XRD and resistivity

As shown in Fig. 1(a), $EuMnSb_2$ crystallizes in an orthorhombic layered structure with the space group of *Pnma* featured by stacking of layers of Eu, MnSb, and Sb zigzag chains alternatively along a axis [6,13]. Figure 1(b) displays the powder XRD diffraction patterns of $EuMn_{1-x}Zn_xSb_2$ ($0 \leqslant x \leqslant 1$), which can be well refined based on the crystal structure of $EuMnSb_2$. The refined lattice parameters a, b, c are plotted against Zn content x in Figs. 1(c)–1(e), respectively. With the increase of x, a first increases slightly from
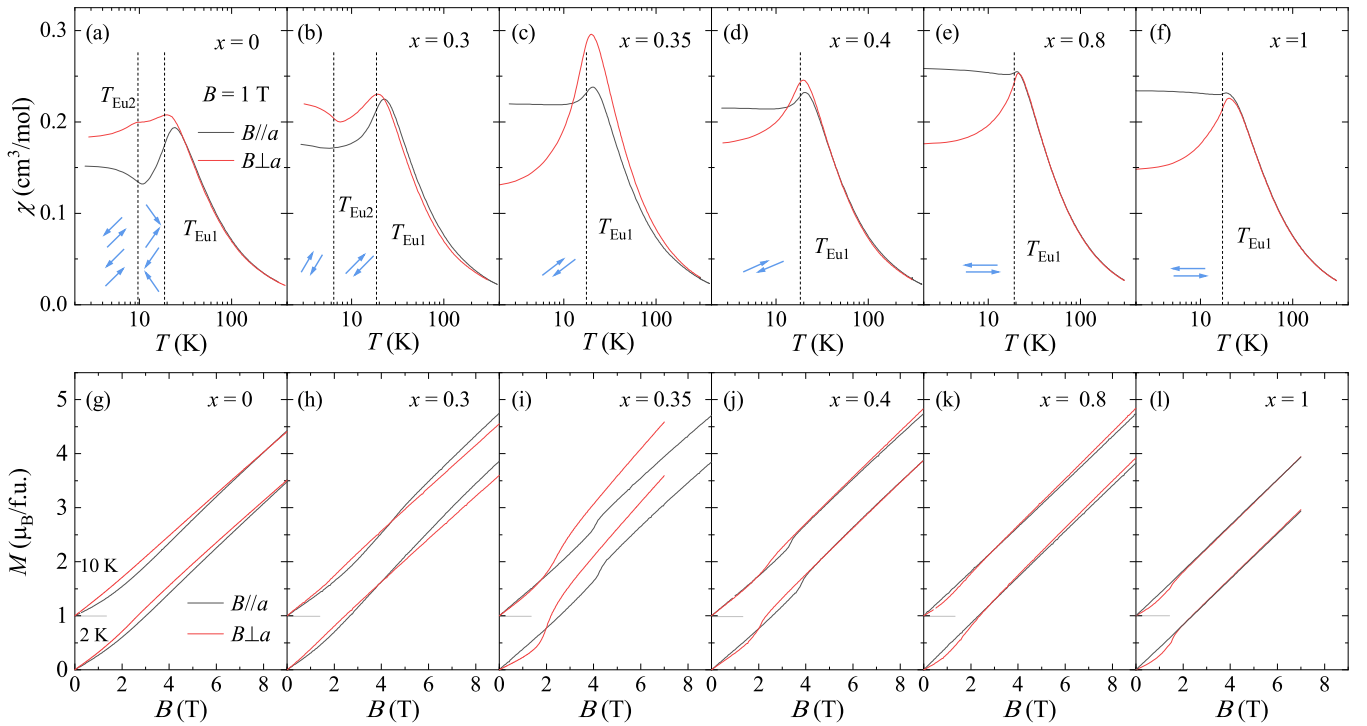
FIG. 2. [(a)–(f)] Temperature dependence of magnetic susceptibility of typical $EuMn_{1-x}Zn_xSb_2$, measured under a field of 1 T with $B \parallel a$ (black line) and $B \perp a$ (red line). Dash lines denote the T_{Eu1} and T_{Eu2}, which are the AFM and spin reorientation transition temperatures of Eu moments, respectively. [(g)–(l)] The corresponding M vs B curves measured at 2 and 10 K, respectively. The data set of 10 K is shifted upward by 1 μ_B/f.u. as marked by the gray lines.

$x = 0$ to $x = 0.14$, then decreases almost linearly from $x = 0.14$ to $x = 1$, implying that the substitution of Mn^{2+} (0.80 Å) by Zn^{2+} (0.74 Å) induces shrinkage of crystal structure as expected for the Vegard's law [14]. The decrease of a is further evidenced by the systematic shift of (600) peak to a higher angle with increasing x [right panel of Fig. 1(b)]. Compared with $EuMnSb_2$, the amplitude of the shrinkage of a is 0.9% for $EuZnSb_2$. However, the in-plane lattice parameters b and c exhibit a nonmonotonic doping dependence, which increases slightly from $x = 0$ to $x = 0.14$ and then exhibits a quick decrease in the doping range of $0.14 \leqslant x \leqslant 0.4$ and follows by a slow increase with further doping, forming a minimum at $x \sim 0.4$. Note that c/b almost keeps intact in the entire doping range, as illustrated by Fig. S1(b) in Ref. [12]. The origin of the nonmonotonic x dependence of b and c is unclear. Actually, the variation of b and c is marginal, and therefore the nonmonotonic dependence could be fragile and easily affected by other sources like the magnetic structure.

Figure 1(f) shows the temperature dependence of in-plane electrical resistivity $\rho(T)$ for $EuMn_{1-x}Zn_xSb_2$ single crystals, which are normalized by the resistivity at room temperature (0.2–0.9 mΩ cm). $\rho(T)$ curves are shifted vertically for clarity. All samples exhibit a metallic behavior above ∼20 K with a residual resistivity ratio (RRR) of ∼5. The anomalies corresponding to the magnetic transitions of Eu moments are shown at low temperatures [6]. To determine the magnetic transition temperatures of Eu, the first derivative of resistivity with respect to temperature $[d\rho(T)/dT]$ is plotted in the inset of Fig. 1(f). From the comparison between the resistivity and magnetization data in Fig. 4, T^ρ_{Eu1} and T^ρ_{Eu2} can be defined as

the minimum and maximum of $d\rho(T)/dT$ curves, as marked by the black dots and inverted triangle in the inset of Fig. 1(f), respectively. From the inset of Fig. 1(f), we can see that T^ρ_{Eu1} exhibits a weak nonmonotonic doping dependence, implying that Zn doping does not significantly alter the magnetic coupling between Eu moments. It is worth noting that the crystal structure and transport properties of $EuMnSb_2$ are sensitive to the chemical stoichiometry of the single crystal grown by different methods. Specifically, in the previous experiments of $EuMnSb_2$ single crystals, both tetrahedral and orthogonal structures were reported, and metallic/semiconducting behavior was shown in the transport properties [6,7,9,13,15]. In this work, all $EuMn_{1-x}Zn_xSb_2$ crystallize in the same orthogonal structure and exhibit a metallic resistivity with a similar RRR, indicating a minor chemical stoichiometric effect and, therefore intrinsic doping dependence of physical properties.

B. Magnetization

Figures 2(a)–2(f) show the temperature-dependent magnetic susceptibilities of $EuMn_{1-x}Zn_xSb_2$. The data were collected with a magnetic field of 1 T applied along the a axis (out-of-plane direction) and bc plane (in-plane direction). The subscript $\parallel$ ($\perp$) denotes the data measured with $B \parallel a$ ($B \perp a$) throughout this paper. There is no obvious bifurcation between the magnetization measured in zero-field-cooled (ZFC) and field-cooled (FC) modes for all the $EuMn_{1-x}Zn_xSb_2$ crystals, and only ZFC data are shown in this paper.

Because of the large effective moment of Eu^{2+} ($g\sqrt{S(S+1)} = 7.94\mu_B$ with $S = \frac{7}{2}$), the paramagnetic signal

TABLE I. Doping dependence of magnetic parameters of $EuMn_{1-x}Zn_xSb_2$ for both $B \parallel a$ and $B \perp a$. T_{Eu1} and T_{Eu2} are obtained from $\chi(T)$. T_{Mn} is defined as the peak of $C_p(T)$. The critical field for the spin-flop transition B_{sf} is defined as the maximum of $dM(B)/dB$. The Curie constant (C) and Curie-Weiss temperature (T_θ) are obtained by the Curie-Weiss fit. μ_{eff} is calculated from the Curie constant by $\mu_{eff} = \sqrt{8C}$. μ_{Mn} is calculated by $\mu_{eff}^2 = \mu_{Eu}^2 + (1-x)\mu_{Mn}^2$ by assuming that Eu^{2+} has a theoretical free-ion moment of $\mu_{Eu} = 7.94\mu_B$ for all x.

x	Field direction	T_{Eu1} (K)	T_{Eu2} (K)	T_{Mn} (K)	B_{sf} (T)	C (cm^3 K mol^{-1})	T_θ (K)	μ_{eff} (μ_B/f.u.)	μ_{Mn} (μ_B/Mn)
0	$B \parallel a$	19.08	9.58	326	3.92	8.36	−17.68	8.17	1.92
	$B \perp a$	17.58	10.29		2.48	8.35	−20.40	8.17	1.92
0.3	$B \parallel a$	18.30	6.28	245	3.35	8.86	−16.70	8.42	2.80
	$B \perp a$	16.07	6.57		1.83	9.22	−39.78	8.59	3.91
0.35	$B \parallel a$	17.58	-	-	4.26	9.56	−33.56	8.74	4.54
	$B \perp a$	16.00	-	-	2.04	9.43	−15.99	8.68	4.36
0.4	$B \parallel a$	18.07	-	-	3.82	9.07	−22.36	8.52	3.98
	$B \perp a$	16.29	-	-	2.10	9.06	−29.67	8.52	3.98
0.6	$B \parallel a$	19.56	-	-	-	8.74	−11.24	8.36	4.15
	$B \perp a$	19.56	-	-	1.70	9.00	−25.82	8.49	4.73
0.8	$B \parallel a$	19.57	-	-	-	8.22	−7.02	8.11	3.68
	$B \perp a$	19.57	-	-	1.62	8.10	−6.38	8.05	2.93
1	$B \parallel a$	17.51	-	-	-	8.16	−7.89	8.08	-
	$B \perp a$	17.51	-	-	1.55	8.12	−8.39	8.06	-

of Eu^{2+} is much stronger than that of Mn^{2+}. It has already been evidenced that the magnitude of magnetic susceptibility for Eu-based 112 compounds ($EuMnSb_2$ and $EuZnSb_2$) is about one order larger than that of Eu-free counterpart ($SrMnSb_2$, $CaMnSb_2$, and $YbMnSb_2$) [6,16–19]. Thus the magnetic susceptibilities of $EuMn_{1-x}Zn_xSb_2$ are dominated by Eu moments, and the magnetic transition of Mn is hidden and cannot be detected by the magnetic susceptibility [6]

The magnetic signal of Eu moments is manifested as a Curie-Weiss behavior at high temperatures and successive magnetic transitions at low temperatures [Figs. 2(a)–2(f)]. As shown in Fig. S2 in Ref. [12], the high-temperature part of $1/\chi(T)$ vs T curves exhibits a linear behavior, which can be well fitted by the Cuire-Weiss law: $\chi(T) = \frac{C}{T - T_\theta}$, where T_θ is the Curie-Weiss temperature and $C = \frac{N_A \mu_{eff}^2}{3k_B}$ is the Curie constant related to the effective moments μ_{eff} by $\mu_{eff} = \sqrt{8C}$ [20]. The obtained μ_{eff} and related magnetic parameters for both $B \parallel a$ and $B \perp a$ are listed in Table I. As shown in Table I and Fig. S3(a) [12], Both $\mu_{eff,\parallel}$ and $\mu_{eff,\perp}$ exhibit a dome-like doping dependence with a weak anisotropy, where μ_{eff} values for $x = 0$ and 1 are close to the theoretical effective moment of Eu^{2+} (7.94 μ_B), while significantly enhanced effective moments with maximum values of $\mu_{eff,\parallel} = 8.74\mu_B/\mu_{eff,\perp} = 8.68\mu_B$ are observed for $x = 0.35$, which can be attributed to the Curie-Weiss contribution of Mn^{2+} moments.

The magnetic susceptibility $\chi(x)$ of $EuMn_{1-x}Zn_xSb_2$ is composed of two contributions arising from Eu^{2+} and Mn^{2+}, respectively [20],

$$\chi(x) = \chi_{Eu} + (1-x)\chi_{Mn}. \quad (1)$$

By assuming a free-ion moment of $\mu_{Eu} = 7.94\mu_B$ for Eu^{2+} and a similar T_θ, we can write Eq.(1) as

$$\mu_{eff}^2(x) = \mu_{Eu}^2 + (1-x)\mu_{Mn}^2 = 7.94^2 + (1-x)\mu_{Mn}^2. \quad (2)$$

The effective moment associated with Mn can be estimated by Eq.(2). The results are shown in Table I and Fig. S3(b) in Ref. [12], where μ_{Mn} increases linearly as a function of

Zn content x and reaches 4.54 μ_B at $x = 0.35$, and decreases slightly with further doping. The estimated μ_{Mn} in $EuMn_{1-x}Zn_xSb_2$ with $x \geqslant 0.35$ is close to that determined by neutron measurements in $EuMnSb_2$ [7–10], indicating the absence of long-range Mn ordering. Then, the domelike doping dependence of total effective moment $\mu_{eff}(x)$ could be understood in terms of the increase of μ_{Mn} in the combination of the decrease of Mn concentration as Zn content x increases. In the underdoped regime, as the suppression of long-range AFM ordering of Mn by Zn doping, the increase of free μ_{Mn} moments leads to the increase of $\mu_{eff}(x)$ values. In the overdoped samples with a similar μ_{Mn}, the reduction of Mn concentration leads to the decrease of $\mu_{eff}(x)$, resulting in a dome-like $\mu_{eff}(x)$ curve.

For the low-temperature magnetic susceptibilities, two magnetic transitions can be identified for $x \leqslant 0.3$, which can be assigned to the antiferromagnetic and spin reorientation transitions, respectively. Two magnetic transitions of Eu sublattice have been reported in $EuMnSb_2$ and $Eu_{1-x}Sr_xMnSb_2$ at $x = 0.2/0.5$ [9,10]. T_{Eu1} and T_{Eu2} are defined as the peak and upturn of $d(\chi T)/dT$ [21], respectively, as indicated by the vertical dash lines in Figs. 2(a)–2(f). The details for the definition of magnetic transition temperatures from various measurements can be found in Fig. 4. However, when $x > 0.3$, only the antiferromagnetic transition is shown. The evolution of T_{Eu1} and T_{Eu2} for both $B \parallel a$ and $B \perp a$ are summarized in Table I. As shown in Table I and Fig. 5, $T_{Eu1,\parallel}$ exhibits a weak nonmonotonic doping dependence. As x increases, $T_{Eu1,\parallel}$ decreases slightly from 19.08 K ($x = 0$) to 17.58 K ($x = 0.35$), increases back to 19.56 K ($x = 0.6$), and eventually decreases to 17.51 K ($x = 1$). $T_{Eu1,\perp}$ exhibits a similar doping dependence behavior with a remarkable anisotropy for $x \leqslant 0.4$. T_{Eu2} decreases with increasing x, and cannot be detected when $x > 0.3$. In addition, at low temperatures, the magnitude of the susceptibilities gradually changes from $\chi_\parallel(T) < \chi_\perp(T)$ to $\chi_\parallel(T) > \chi_\perp(T)$ with x increasing, suggesting that the Eu moments gradually rotates from a direction close to a axis in $EuMnSb_2$ to bc plane in $EuZnSb_2$ [10,16].
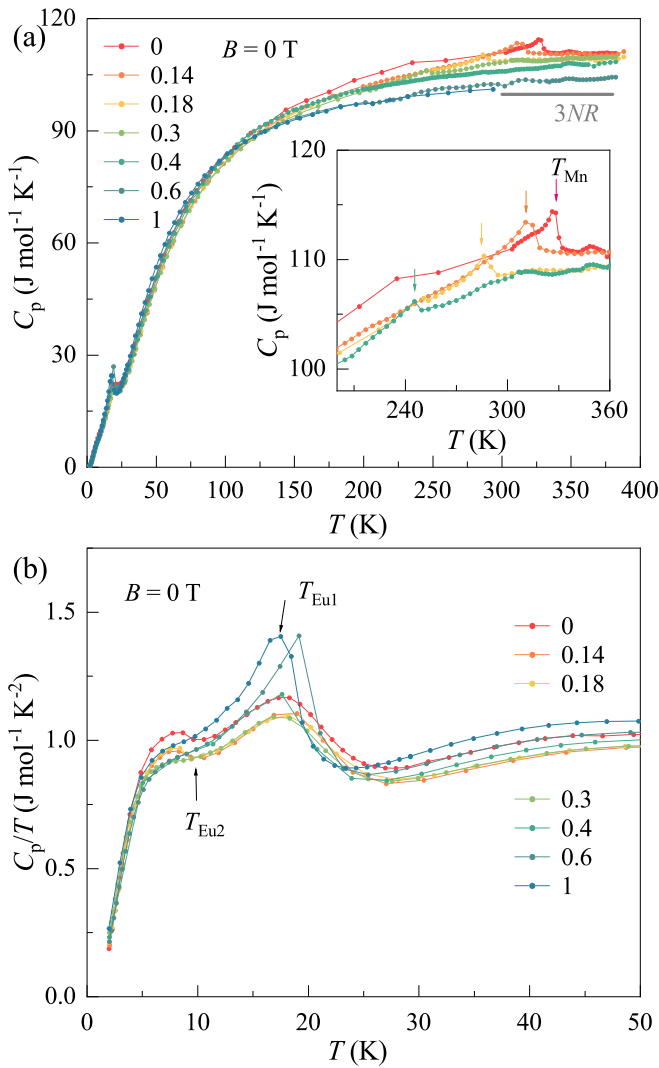
FIG. 3. (a) Temperature dependence of specific heat for EuMn$_{1-x}$Zn$_x$Sb$_2$ at zero field. The inset of (a) and (b) shows the enlarged plot of the high-temperature and low-temperature parts of specific heat, respectively. The arrows mark the magnetic transition temperatures.

Figures 2(g)–2(l) show the field dependence of magnetization $M(B)$, measured at 2 K and 10 K in magnetic fields up to 9 T, the black and red lines represent the magnetization measured with $B \parallel a$ and $B \perp a$, respectively. All $M(B)$ curves exhibit a nearly linear field dependence with a slope change or steplike increase at 3–4 T, indicating the dominated AFM coupling with a spin-flop transition. The saturation field is estimated to be ~20 T at 2 K by linear extension to the theoretical effective moment of Eu^{2+}, implying a strong AFM coupling between Eu moments [9,16,22]. The critical field of the spin-flop transition B_{sf} is defined as the peak of $dM(B)/dB$, and the obtained B_{sf} is shown in Table I and Fig. S4 [12]. The applied field ($B = 1$ T) for $\chi(T)$ measurements in Figs. 2(a)–2(f) is lower than B_{sf}, indicating that $\chi(T)$ measurements probe the AFM phase of Eu moments. It is worth noting that the spin-flop transition is manifested as a slope change for $x = 0$ and 0.3, while a steplike increase for $x = 0.35$ and 0.4 [Figs. 2(g)–2(l)]. As shown in Fig. S5

[12], a sizable hysteresis between the field-increasing and field-decreasing runs of $M_\parallel(B)$ curves for $x = 0.35$ and 0.4, implying a first-order phase transition.

C. Magnetic structure of Eu sublattice

For $x = 0$, both $\chi_\parallel(T)$ and $\chi_\perp(T)$ decrease with decreasing the temperature for $T_{Eu2} < T < T_{Eu1}$, implying a canted AFM order of Eu sublattice. $\chi_\parallel(T)$ increases while $\chi_\perp(T)$ decreases upon cooling across T_{Eu2}, indicative of a spin reorientation transition. Magnetic structure of EuMnSb$_2$ with similar $\chi(T)$ curves have been given by a comprehensive neutron study [10]. Specifically, for $T_{Eu2} < T < T_{Eu1}$, Eu moments order into a canted AFM with Eu moments confined within the ac plane with a "+−+−" component along the a axis and a "++−−" component along the c axis. At 12 K, $\mu_{Eu} = 4.7(2)$ μ_B with a canting angle of 31°. When $T < T_{Eu2}$, Eu moments are arranged in a canted AFM ordering with a "+−+−" component along both a and b axes and a "++−−" component along the c axis. At 5 K, $\mu_{Eu} = 5.6(4)$ μ_B with components of 2.4(4) μ_B, 4.3(2) μ_B, and 2.6(2) μ_B lying along a, b, and c, respectively. Our EuMnSb$_2$ single crystal is regarded to have the same magnetic structure.

When we further increase x to be 0.3, both $\chi_\parallel(T)$ and $\chi_\perp(T)$ decrease for $T_{Eu2} < T < T_{Eu1}$ with $\chi_\parallel(T) < \chi_\perp(T)$, similar to the case of EuMnSb$_2$. The only difference is that the Eu moments of EuMn$_{0.7}$Zn$_{0.3}$Sb$_2$ tend to the bc plane a bit more than that of EuMnSb$_2$ since the difference between $\chi_\parallel(T)$ and $\chi_\perp(T)$ is smaller for EuMn$_{0.7}$Zn$_{0.3}$Sb$_2$. For $T < T_{Eu2}$, an obvious upturn of $\chi(T)$ is observed when $B \perp a$, opposite to $B \parallel a$ in EuMnSb$_2$, suggesting an opposite direction for spin reorientation.

For $0.35 \leqslant x \leqslant 1$, only an AFM transition at T_{Eu1} is observed in $\chi(T)$. $\chi_\parallel(T) > \chi_\perp(T)$ below T_{Eu1} indicates that Eu moments are oriented close to bc plane. The canting angle of Eu moments can be inferred from the anisotropy of the spin-flop transition. Anomaly corresponding to spin-flop transition is observed both in $M_\parallel(B)$ and$M_\perp(B)$ for $x = 0.35$ and 0.4, indicating the canted AFM structure. The smaller $B_{sf,\parallel}/B_{sf,\perp}$ ratio (Table I) indicates the canting angle of $x = 0.4$ is slightly larger than that of $x = 0.35$ [23]. The magnetization for $x = 0.8$ and 1 is consistent with a typical collinear AFM with moments lying in the bc plane.

D. Specific heat

As mentioned previously, the signal of Mn moments cannot be detected from magnetization. To understand the behavior of Mn moments, specific heat measurements are performed to extract Mn ordering temperature T_{Mn}. As shown in the inset of Fig. 3(a) and also Fig. 3(b), three anomalies, marked by the arrows, are observed in the specific heat curve of EuMnSb$_2$ at $T = 326$, 17.67, and 10.11 K. The two anomalies at low temperature, i.e., 17.67 and 10.11 K, are consistent with T_{Eu1} and T_{Eu2} determined by about magnetization measurements as shown in the previous section. Like magnetization measurements, the specific-heat jump corresponding to T_{Eu1} does not show significant doping dependence. The anomaly corresponding to the spin reorientation at T_{Eu2} is only observed for low-doping with $x = 0, 0.14, 0.18$,
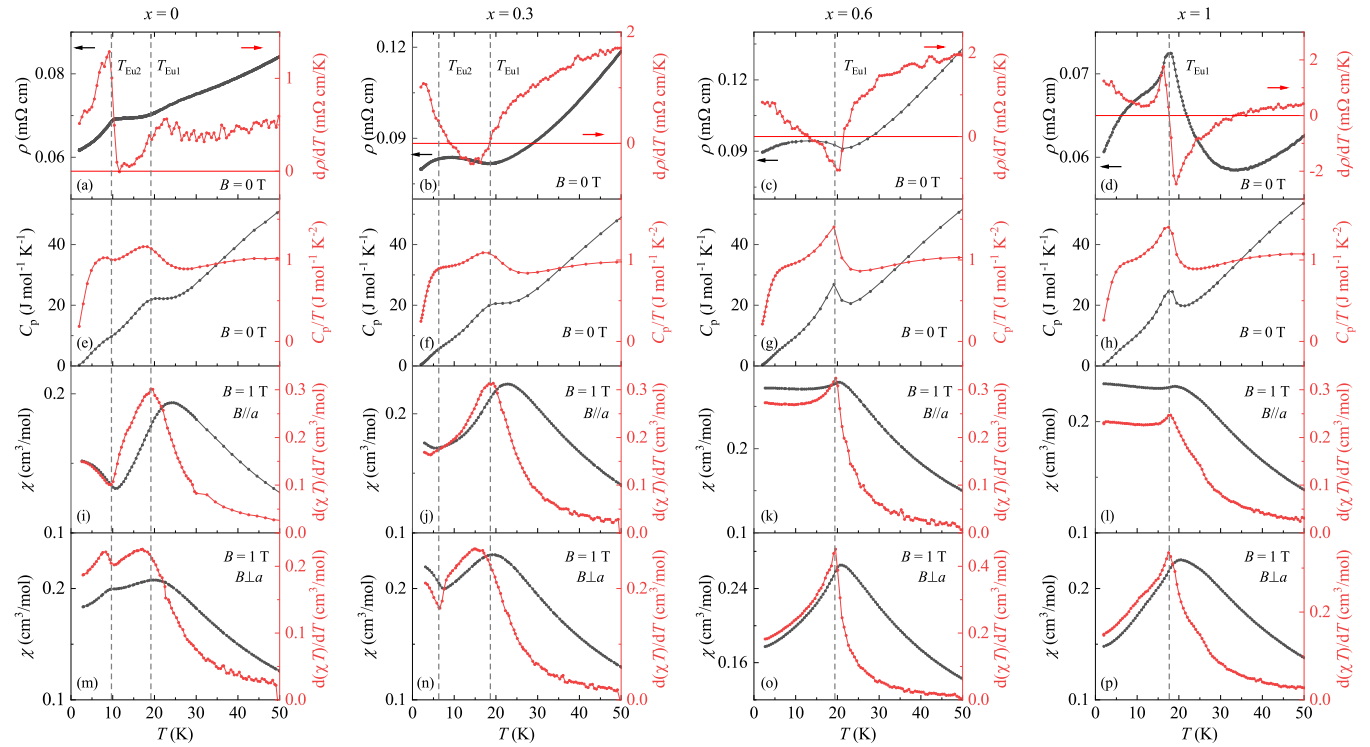
FIG. 4. Criteria used to determine the transition temperatures in EuMn$_{1-x}$Zn$_x$Sb$_2$. [(a)–(d)] The zero-field resistivity and its derivative. [(e)–(h)] Specific heat C_p and C_p/T. Magnetic susceptibility and the derivative $d(\chi T)/dT$ of susceptibility under a field of 1 T with $B \parallel a$ [(i)–(l)] and $B \perp a$ [(m)–(p)]. Vertical lines mark the peak and valley of $d(\chi_\parallel T)/dT$ curves, which represent T_{Eu1} and T_{Eu2}, respectively.

and 0.3. As for the anomaly at high temperatures [inset of Fig. 3(a)], it is attributed to the AFM ordering of Mn. The peak of the specific heat jump is marked as T_{Mn} in the figure. $T_{Mn} = 326$ K at $x = 0$ is in good agreement with that determined by the neutron measurements [10]. When x increases, specific-heat jump corresponding to T_{Mn} gradually shifts to low temperatures and eventually becomes invisible for $x > 0.3$.

As shown in Figs. 3(a) and S6 [12], the magnitude of the high-temperature specific heat decreases as x increases, and the room-temperature specific heat gradually approaches the Dulong-Petit value of $3NR$, where $N = 4$ is the atomic number per chemical formula and R is the universal gas constant 8.314 J mol^{-1} K^{-1}. Since Zn can be taken as the nonmagnetic analogy of Mn due to the similar molar mass, the decrease of high-temperature $C_p(T)$ mainly arises from the suppression of the magnetic entropy of Mn by Zn doping. The magnetic contribution to specific heat is maximum around Neel temperature T_N in an antiferromagnet, which decreases as temperature increases, eventually becoming very small at $T \gg T_N$ [24]. $C_p(T)$ with a magnitude higher than the Dulong-Petit limit for $0 \leqslant x \leqslant 0.4$ indicate that magnetic fluctuations of Mn moments could persist to 375 K, a temperature significantly higher than T_N (245–326 K). A similar phenomenon has also been observed in BaMn$_2$Sb$_2$ with a similar crystal structure [25]. Note that magnetic fluctuation of $x = 0.4$ also persists to 375 K, where the anomaly corresponding to Mn ordering is invisible. This result indicates that Mn ordering is likely present in $x = 0.4$, and the absence of specific heat anomalies might be induced by the broad magnetic transition.

E. Phase diagram and discussion

To clarify the definition of the magnetic transitions and compare the transitions inferred from different measurements, the resistivity, specific heat, magnetic susceptibility, and corresponding derivatives for four typical samples ($x = 0, 0.3, 0.6$, and 1) are plotted in Fig. 4. T_{Eu1} is defined as the valley of $d\rho/dT$, peak of C_p/T, and peak of $d(\chi T)/dT$ curves, and T_{Eu2} is defined as the peak of $d\rho/dT$, upturn of C_p/T, and upturn of $d(\chi T)/dT$ curves. From Fig. 4, we can see that T_{Eu1} and T_{Eu2} defined from various measurements are in good agreement with each other, especially for the specific heat and magnetization measurements. According to the theoretical argument of Fisher, the variation of the magnetic specific heat of a simple antiferromagnet should be similar to the behavior of $d(\chi T)/dT$ and $d\rho/dT$ near the magnetic transition temperature [21,26]. It is evidented that C_p/T curves resemble to those of $d(\chi_\parallel T)/dT$, consistent with the Fisher's relation [21]. There is a slight difference between C_p/T and $d(\chi_\perp T)/dT$ due to the suppression of T_N by a perpendicular field, which will be discussed in the following paragraph. However, it can be seen from Figs. 4(a)–4(d) that Fisher's relation between C_p/T and $d\rho/dT$ is only applicable in $x = 1$, possibly due to the existence of complex scattering in doped samples with two types of magnetic ions.

The magnetic transitions extracted from the magnetization for $B \parallel a$ and $B \perp a$ and zero-field specific heat measurements are summarized in magnetic phase diagrams as shown in Figs. 5(a) and 5(b), respectively, where the contour plots of $d(\chi T)/dT$ are shown to highlight the magnetic transitions. For low doping $x \leqslant 0.3$ with $B \parallel a$, there are three magnetic
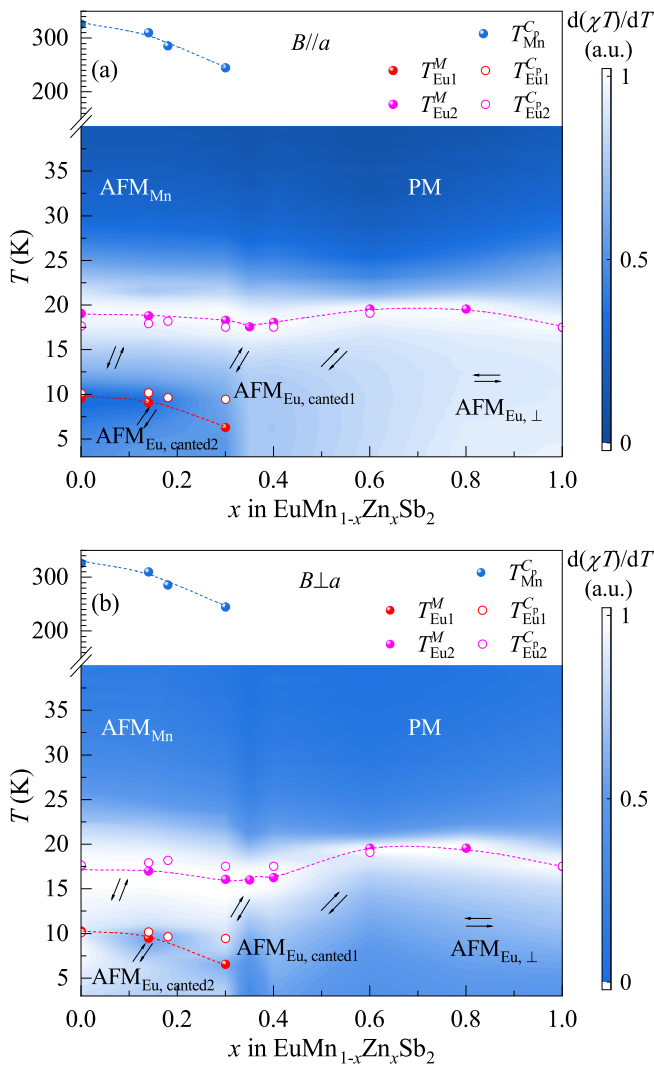
FIG. 5. (a) and (b) are magnetic phase diagrams of EuMn$_{1-x}$Zn$_x$Sb$_2$ as functions of Zn content x and temperature for $B \parallel a$ and $B \perp a$, respectively. The color map represents $d(\chi T)/dT$ in the parameter spaces of Zn content x and temperature. Black arrows are schematic illustrations of the orientation of Eu moments. Dash lines are guides to the eyes. Note that the magnetization data were measured in a magnetic field of 1 T while the specific heat measurements were performed in the absence of the magnetic field. The superscript of magnetic transition temperature denotes the experimental method.

transitions (T_{Mn}, T_{Eu1}, and T_{Eu2}) observed in EuMn$_{1-x}$Zn$_x$Sb$_2$, which separate the phase diagram into a paramagnetic phase (PM), AFM phase of Mn (AFM$_{Mn}$), two canted AFM phases of Eu (AFM$_{Eu,canted1}$ and AFM$_{Eu,canted2}$) [6]. As x increases from 0 to 0.3, T_{Mn} decreases from 326 to 245 K, T_{Eu1} decreases slightly from 19.08 to 18.30 K; T_{Eu2} decreases from 9.58 to 6.28 K. Note that T_{Eu2} is visible in crystals with detectable T_{Mn} in specific-heat measurements. The evolution of Eu orientation is schematically illustrated by the arrows in Fig. 5, which gradually titles from a direction close to the a axis to the bc plane. This results from the decrease of Eu-Mn coupling induced by Zn doping. At higher doping $x > 0.3$, only T_{Eu1} is detectable whereas both T_{Mn} and T_{Eu2} are invisible. The AFM phase with Eu moment oriented along bc plane is denoted as

AFM$_{Eu,\perp}$ since the Mn moments are too weak to drive the Eu moments towards a axis. As shown in Fig. 5(b), the magnetic phase diagram for $B \perp a$ resembles that for $B \parallel a$, and the main difference between the phase diagram for $B \parallel a$ and $B \perp a$ is the anisotropy of T_{Eu1}^M in the underdoped regime ($0 \leqslant x \leqslant 0.4$), as evidenced by the location of T_{Eu1}^M with respect to $T_{Eu1}^{C_p}$ determined by the zero-field specific heat [Figs. 5(a) and 5(b)]. $T_{Eu1,\parallel}^M$ and $T_{Eu1,\perp}^M$ are plotted against Zn content x in Fig. S7 to highlight the anisotropy for $0 \leqslant x \leqslant 0.4$ [12]. Since Eu ions in EuMn$_{1-x}$Zn$_x$Sb$_2$ are divalent with $S = 7/2$ and $L = 0$, the single-ion anisotropy is not expected as observed in $0.6 \leqslant x \leqslant 1$. Thus the anisotropy of T_{Eu1}^M can be attributed to the interaction of magnetism between Eu and Mn. Therefore T_{Eu1} exhibits a different doping dependence in regimes with and without Mn ordering, which is manifested as a nonmonotonic T_{Eu1} vs x curve with a minimum around $x = 0.4$.

The spin reorientation transition is a common phenomenon in layered oxypnictide containing two AFM sublattices such as RMnAsO (R = Ce or Nd) [27,28], RMnSbO (R = Ce or Pr) [29,30], and RFeAsO (R = Ce, Pr, or Nd) [31,32]. The spin reorientation transition of transition metal Mn/Fe is induced by the occurrence of the AFM ordering of rare earth at low temperatures, which drives the Mn/Fe moment parallel to its moment direction. In the magnetic phase diagram of Eu$_{1-x}$Sr$_x$MnSb$_2$ [9], the Eu moment direction changes from the in-plane direction to the out-of-plane direction while the Mn moment remains along the out-of-plane direction, which can be understood in the framework of the competition between the Mn-Mn, Eu-Eu, and Eu-Mn coupling. The Mn-Mn coupling results in an out-of-plane direction of Mn moments, the Eu-Eu coupling leads to an in-plane preferred orientation of Eu moments, and the Eu-Mn coupling induces a tendency toward a parallel arrangement of Eu and Mn moments. With increasing x in the case of Eu$_{1-x}$Sr$_x$MnSb$_2$, the Eu moments are gradually polarized to the direction of Mn since the Eu-Eu coupling is weakened by Sr doping while the Mn-Mn coupling remains unchanged. Our study on EuMn$_{1-x}$Zn$_x$Sb$_2$ can serve as the complementary investigation of Eu$_{1-x}$Sr$_x$MnSb$_2$, and the magnetic phase diagram can be understood in the similar scenario. Here, the Mn-Mn coupling is weakened by Zn doping; therefore, the competition between the Mn-Mn and Eu-Mn coupling plays a leading role. At low doping of Zn, the Mn-Mn coupling is strong, and then the Eu-Mn coupling results in out-of-plane preferred Eu moments. As Zn content x increases, the Mn-Mn coupling is weakened, resulting in the decrease of T_{Mn}. Further, the Eu moments change from out-of-plane to in-plane orientation, and T_{Eu1} remains almost unchanged since the weakened Eu-Mn coupling can not drive the Eu moments anymore. Note that the orientation of Mn moment, especially for high doping, is unknown at present, which could also exhibit a spin reorientation transition since the Mn-Mn coupling is weakened by Zn doping. Therefore the spin reorientation transition for Mn moments can be driven by the Eu moments due to the Eu-Mn coupling. Neutron measurement is required to clarify the detailed magnetic structure for the Eu and Mn sublattices.

Our work shows a doping-dependent spin reorientation of the Eu moment through the Eu-Mn coupling. Because Zn doping can effectively manipulate the Eu moment direction without disturbing the Eu-Eu coupling, which could be an

effective way to manipulate the physical properties sensitive to Eu magnetism, such as interlayer transport and topological state. In addition, the controversy about the reported Eu sublattice in $EuMnSb_2$ can also be understood in this scenario, where the canting of Eu moment is strongly dependent on the Mn-Mn coupling strength, which could be different in single crystals with different Mn vacancies.

IV. CONCLUSIONS

A series of $EuMn_{1-x}Zn_xSb_2$ ($0 \leqslant x \leqslant 1$) single crystals were successfully synthesized by the flux method, and the magnetic phase diagrams of $EuMn_{1-x}Zn_xSb_2$ along two magnetic field orientations are established based on the results of magnetization and specific heat measurements. While the antiferromagnetic transition temperature of Eu almost keeps intact, a Zn doping dependence of the Eu orientation is observed, which arises from the strong coupling between the magnetism between Eu and Mn. Our study shows that the

magnetic structure of rare earth elements can be manipulated through interaction between two magnetic sublattices, which paves a new avenue for manipulating the magnetic states of antiferromagnets.

[1] T. Jungwirth, J. Sinova, A. Manchon, X. Marti, J. Wunderlich, and C. Felser, Nat. Phys. **14**, 200 (2018).

[2] L. Šmejkal, T. Jungwirth, and J. Sinova, Phys. Status Solidi RRL **11**, 1700044 (2017).

[3] S. Klemenz, S. Lei, and L. M. Schoop, Annu. Rev. Mater. Res. **49**, 185 (2019).

[4] Z. L. Sun, A. F. Wang, H. M. Mu, H. H. Wang, Z. F. Wang, T. Wu, Z. Y. Wang, X. Y. Zhou, and X. H. Chen, npj Quantum Mater. **6**, 94 (2021).

[5] Z. Sun, H. Wang, A. Wang, B. Lei, W. Zhuo, F. Yu, X. Zhou, J. Ying, Z. Xiang, T. Wu, and X. Chen, Adv. Funct. Mater. **32**, 2202188 (2022).

[6] L. Zhang, Z. Sun, A. Wang, Y. Xia, X. Mi, L. Zhang, M. He, Y. Chai, T. Wu, R. Wang, X. Zhou, and X. Chen, Phys. Rev. B **104**, 205108 (2021).

[7] D. Gong, S. Huang, F. Ye, X. Gui, J. Zhang, W. Xie, and R. Jin, Phys. Rev. B **101**, 224422 (2020).

[8] J.-R. Soh, P. Manuel, N. M. B. Schröter, C. J. Yi, F. Orlandi, Y. G. Shi, D. Prabhakaran, and A. T. Boothroyd, Phys. Rev. B **100**, 174406 (2019).

[9] Q. Zhang, J. Liu, H. Cao, A. Phelan, D. Graf, J. F. DiTusa, D. A. Tennant, and Z. Mao, NPG Asia Materials **14**, 22 (2022).

[10] J. M. Wilde, S. X. M. Riberolles, A. Das, Y. Liu, T. W. Heitmann, X. Wang, W. E. Straszheim, S. L. Bud'ko, P. C. Canfield, A. Kreyssig, R. J. McQueeney, D. H. Ryan, and B. G. Ueland, Phys. Rev. B **106**, 024420 (2022).

[11] D. J. Goossens, A. J. Studer, S. J. Kennedy, and T. J. Hicks, J. Phys.: Condens. Matter **12**, 4233 (2000).

[12] See Supplemental Material at http://link.aps.org/supplemental/10.1103/PhysRevB.107.184415 for the inversed susceptibility versus temperature curves, hysteretic isothermal magnetizations, and the detailed magnetic parameters.

[13] C. Yi, S. Yang, M. Yang, L. Wang, Y. Matsushita, S. Miao, Y. Jiao, J. Cheng, Y. Li, K. Yamaura, Y. Shi, and J. Luo, Phys. Rev. B **96**, 205103 (2017).

[14] A. R. Denton and N. W. Ashcroft, Phys. Rev. A **43**, 3161 (1991).

[15] Q. Zhu, Q. Mao, B. Xu, J. Du, M. Chen, J. Yang, B. Chen, C. Cao, H. Wang, and M. Fang, J. Phys.: Condens. Matter **31**, 185701 (2019).

[16] A. Wang, S. Baranets, Y. Liu, X. Tong, E. Stavitski, J. Zhang, Y. Chai, W.-G. Yin, S. Bobev, and C. Petrovic, Phys. Rev. Res. **2**, 033462 (2020).

[17] J. Y. Liu, J. Hu, Q. Zhang, D. Graf, H. B. Cao, S. M. A. Radmanesh, D. J. Adams, Y. L. Zhu, G. Cheng, X. Liu, W. A. Phelan, J. Wei, M. Jaime, F. Balakirev, D. A. Tennant, J. F. DiTusa, I. Chiorescu, L. Spinu, and Z. Q. Mao, Nat. Mater. **16**, 905 (2017).

[18] H. Rong, L. Zhou, J. He, C. Song, J. Huang, C. Hu, Y. Xu, Y. Cai, H. Chen, C. Li, Q. Wang, L. Zhao, Z. Zhu, G. Liu, Z. Xu, G. Chen, H. Weng, and X. J. Zhou, Phys. Rev. B **103**, 245104 (2021).

[19] Y.-Y. Wang, S. Xu, L.-L. Sun, and T.-L. Xia, Phys. Rev. Mater. **2**, 021201(R) (2018).

[20] S. Blundell, *Magnetism in Condensed Matter*, Oxford Master Series in Physics (Oxford University Press, Oxford, New York, 2001).

[21] M. E. Fisher, Philos. Mag. **7**, 1731 (1962).

[22] H. Masuda, H. Sakai, M. Tokunaga, Y. Yamasaki, A. Miyake, J. Shiogai, S. Nakamura, S. Awaji, A. Tsukazaki, H. Nakao, Y. Murakami, T.-h. Arima, Y. Tokura, and S. Ishiwata, Sci. Adv. **2**, e1501117 (2016).

[23] F. Zhu, X. Wang, M. Meven, J. Song, T. Mueller, C. Yi, W. Ji, Y. Shi, J. Ma, K. Schmalzl, W. F. Schmidt, Y. Su, and T. Brückel, Phys. Rev. Res. **2**, 043100 (2020).

[24] A. P. Cracknell and A. O. Tooke, Contemp. Phys. **20**, 55 (1979).

[25] N. S. Sangeetha, V. Smetana, A.-V. Mudring, and D. C. Johnston, Phys. Rev. B **97**, 014402 (2018).

[26] M. E. Fisher and J. S. Langer, Phys. Rev. Lett. **20**, 665 (1968).

[27] Q. Zhang, W. Tian, S. G. Peterson, K. W. Dennis, and D. Vaknin, Phys. Rev. B **91**, 064418 (2015).

[28] N. Emery, E. J. Wildman, J. M. S. Skakle, A. C. Mclaughlin, R. I. Smith, and A. N. Fitch, Phys. Rev. B **83**, 144429 (2011).

[29] Q. Zhang, C. M. N. Kumar, W. Tian, K. W. Dennis, A. I. Goldman, and D. Vaknin, Phys. Rev. B **93**, 094413 (2016).

[30] S. A. J. Kimber, A. H. Hill, Y.-Z. Zhang, H. O. Jeschke, R. Valentí, C. Ritter, I. Schellenberg, W. Hermes, R. Pöttgen, and D. N. Argyriou, Phys. Rev. B **82**, 100412(R) (2010).

[31] T. Shang, L. Yang, Y. Chen, N. Cornell, F. Ronning, J. L. Zhang, L. Jiao, Y. H. Chen, J. Chen, A. Howard, J. Dai, J. D. Thompson, A. Zakhidov, M. B. Salamon, and H. Q. Yuan, Phys. Rev. B **87**, 075148 (2013).

[32] A. Marcinkova, D. A. M. Grist, I. Margiolaki, T. C. Hansen, S. Margadonna, and J.-W. G. Bos, Phys. Rev. B **81**, 064511 (2010).